PAPER

Check for updates

Novel self-assembled metal-phenolic nanoplatforms for triple-negative breast cancer treatment: photothermal-chemotherapy/ferroptosis synergy inducing immunogenic cell death

Bohao Peng,[†][a] Ruoyao Wang,[†][a] Tian Li,[a] Xiaoqing Yu,[a] Zhiyu Wang,[a] Xiyang Zhang,[a] Yuanfeng Tan,[a] Long Cheng[*][bc] and Lu Yang [ID] [*][a]

Triple-negative breast cancer (TNBC) poses a serious threat to women's health. Currently, chemotherapy remains the first-line treatment in the clinic, and more comprehensive treatments are urgently needed to improve the therapeutic efficacy of TNBC. Emerging studies have indicated that photothermal therapy, ferroptosis and immunotherapy also play crucial roles in TNBC treatment. Iron based metal-phenolic networks (MPNs), an emerging class of nanomaterials, are attracting great attention in tumor related research due to their unique structural features. These features endow MPNs with outstanding catalytic efficiency for the Fenton reaction and excellent metal–ligand conversion properties, offering promising prospects for photothermal and photodynamic therapies as well as combined treatment strategies for tumors. In this study, a novel iron-based metal-phenolic nanoplatform, namely MTO-loaded TA/Fe nanocomposites (MFTA), was synthesized. Mitoxantrone (MTO), a commonly used anthracycline, was employed along with ferric chloride ($FeCl_3$) and tannic acid (TA) in the synthesis process. Firstly, TA and $FeCl_3$, two non-photosensitive substances, underwent a coordination reaction to form a blue-black compound TAF, which exhibited ideal photosensitivity. Secondly, through $\pi-\pi$ interactions, TAF and MTO partially quenched the autofluorescence of MTO, leading to a cascade amplification of photothermal conversion in the self-assembled nanoplatforms. The myocardial-protective effect of TA enhanced the safety of MTO-based chemotherapy. Additionally, $FeCl_3$ was partially reduced to ferrous ion (Fe^{2+}) by TA, and the introduction of a large amount of Fe^{2+} could trigger ferroptosis in TNBC. Moreover, the induction of immunogenic cell death in TNBC cells, which was stimulated by photothermal therapy, chemotherapy and ferroptosis, further enhanced the synergistic effect. Finally, this nanoplatform may help improve real-time photoacoustic imaging and assist in treatment monitoring. In summary, the developed nanoplatform offers a novel strategy for the comprehensive treatment of TNBC, holding certain potential for clinical translation.

1. Introduction

Breast cancer is the most frequent neoplasm in women worldwide, seriously threatening women's health.[1–3] Triple-negative breast cancer (TNBC), the most aggressive molecular subtype, is characterized by a high propensity for distant metastasis and a high mortality rate.[4] The absence of effective therapeutic targets and strategies is one of the primary factors contributing to its poor prognosis.[5,6] To date, chemotherapy remains the mainstay of treatment for TNBC. Among chemotherapeutic agents, anthracyclines are important first-line drugs. However, their application is limited by cardiotoxicity and drug resistance mediated by cancer stem cells, which poses a significant challenge to the treatment of patients with TNBC.[7–9]

To overcome the limitations of conventional chemotherapy, novel therapeutic approaches including photothermal therapy (PTT) have demonstrated remarkable potential.[10] As a typical anthracycline chemotherapeutic agent, mitoxantrone (MTO) not only serves as an effective chemotherapeutic drug but also exhibits exceptional photothermal conversion capabilities, with studies reporting strong NIR absorption within the 600–700 nm

[a]*Department of Breast and Thyroid Surgery, The Second Affiliated Hospital of Chongqing Medical University, Chongqing 400010, P. R. China. E-mail: 302118@cqmu.edu.cn*

[b]*Ultrasound Department of the Second Affiliated Hospital, The Second Affiliated Hospital of Chongqing Medical University, Chongqing 400010, P. R. China. E-mail: 304188@hospital.cqmu.edu.cn*

[c]*Chongqing Key Laboratory of Ultrasound Molecular Imaging and Therapy, The Second Affiliated Hospital of Chongqing Medical University, Chongqing 400010, P. R. China*

† These authors contributed equally.

wavelength range.[11,12] PTT utilizes photothermal transduction agents (PTAs) to convert NIR energy into thermal energy, effectively eliminating tumor cells by leveraging their lower thermal tolerance compared to normal tissues. However, MTO's inherent autofluorescence characteristics may compromise its photothermal conversion efficiency.[13] Strategies aim at quenching this fluorescence can significantly enhance both its photothermal performance and the overall efficacy of PTT.[14] In addition to PTT, emerging evidence suggests that TNBC, particularly the luminal androgen receptor subtype, exhibits heightened sensitivity to ferroptosis, an iron-dependent form of programmed cell death that has recently gained substantial attention as a crucial mechanism in TNBC treatment.[15,16] Therefore, the development of MTO-based nanomaterials, through rational design and engineering, may provide a promising platform for integrating chemotherapy, photothermal therapy, and ferroptosis induction, potentially achieving synergistic therapeutic efficacy while minimizing systemic side effects.

Iron based metal-phenolic networks (MPNs), as an emerging class of nanomaterial systems, are receiving extensive attention and in-depth exploration in the field of tumor related research at present.[17–19] Compared with other nanomaterials, iron-based MPNs exhibit superior catalytic efficiency for the Fenton reaction due to their unique structural characteristics.[20] Moreover, their excellent metal–ligand conversion properties significantly enhance light absorption in the UV-Vis-NIR range under laser irradiation, providing highly promising application prospects for photothermal therapy, photodynamic therapy, and combined tumor treatment strategies.[21] In this study, we engineered a novel multifunctional metal-phenolic nanoplatform, namely MFTA, constructed using MTO, ferric chloride (FeCl$_3$) and tannic acid (TA) (Fig. 1A). First, TA can inhibit anthracycline-induced cardiotoxicity by inhibiting oxidative stress, inflammation and apoptotic damage,[22] thereby increasing the physical tolerance to MTO. This property of TA makes it an ideal component for the design of a multifunctional nanoplatform. Secondly, the colorless solution TA and FeCl$_3$ react with each other to form a blue-black compound, TAF. The coordination interaction between ferric ion (Fe^{3+}) and TA affects the incompletely filled d orbital of Fe^{3+} to induce d orbital splitting, resulting in d–d electron transition and light absorption under NIR excitation.[23,24] Consequently, TAF exhibits photothermal conversion efficiency comparable to that of MTO. Furthermore, the π–π interaction between TAF and MTO partially quenches MTO's intramolecular fluorescence under NIR excitation, enhancing the photothermal effect of MFTA and establishing a cascade photothermal enhancement mode (Fig. 1B and C). Thirdly, the combination of FeCl$_3$ and TA partially reduces Fe^{3+} to Fe^{2+}. Upon laser irradiation, the PTT of MFTA can generate a substantial amount of reactive oxygen species (ROS) in TNBC cells,[25] while the abundant Fe^{2+} synergistically promote ferroptosis. Additionally, photothermal therapy, chemotherapy and ferroptosis can stimulate antitumor immunity by inducing immunogenic cell death (ICD) in TNBC cells,[26–29] achieving a novel and synergistic strategy that

integrates multiple treatment modalities for enhanced TNBC therapy (Fig. 1D).

Currently, the most effective treatment modalities for TNBC include chemotherapy, PTT, ferroptosis, and immunotherapy. In this study, we present a novel self-assembled cascade-enhanced photosensitive nanoplatform that integrates these four mainstream treatment approaches. Moreover, the nanoplatform exhibits photoacoustic conversion capabilities, enabling its application in diagnosis through photoacoustic imaging. Thus, this nanoplatform offers an novel strategy for integrated diagnosis and treatment, providing a better solution to the complex challenges in TNBC therapy.

2. Materials and methods

2.1 Materials

Ferric chloride (FeCl$_3$), tannic acid (TA), and mitoxantrone (MTO) were sourced from MedChemExpress (MCE). The glutathione (GSH)/oxidized glutathione disulfide (GSSG) assay kit, the adenosine triphosphate (ATP) assay kit, the Annexin V-fluorescein isothiocyanate (FITC)/propidium iodide (PI) apoptosis assay kit, the cell counting kit-8 (CCK-8), 4′,6-diamidino-2-phenylindole (DAPI), 2,7-dichlorofluorescein diacetate (DCFH-DA) and C11-BODIPY fluorescent probes were obtained from Beyotime Biotechnology Co., Ltd. The remaining reagents were commercially accessible chemical reagents. Anti-calreticulin (CRT), anti-high-mobility group protein 1 (HMGB-1), and anti-CD8α rabbit polyclonal antibodies were procured from the Servicebio Technology. Regenerated cellulose dialysis membranes with molecular weight cut-off (MWCO) values of 500 or 8000 Da were supplied by Shanghai Yuanye Biotechnology Co., Ltd (Shanghai, China). The PURIST UV ultrapure water system (Riefel Bioscience Co., Ltd, Shanghai, China) was used to purify the water used in all experiments, with a resistivity greater than 18.2 MΩ cm.

2.2 Synthesis of MFTA nanoplatforms

MTO-loaded TA/Fe^{3+} nanocomposites (MFTA) were established following previously described techniques.[36] MTO·2HCl (5.17 mg, MR = 517.4) was dissolved in 100 μL of methanol and neutralized with 3 μL of trimethylamine to obtain a hydrophobic MTO. Then, TA (17.01 mg, MR = 1701.2) was dissolved in anhydrous ethanol (100 μL) and combined with MTO solution at a molar ratio of 1 : 1 while stirring. The FeCl$_3$·6H$_2$O (MR = 270.2) aqueous solution (1 mg mL^{-1}, 27 mL) was added to the mixture and agitated overnight to evaporate methanol and anhydrous ethanol solvent. The mixture was then centrifuged at 13 000 rpm for 20 min at 4 °C to yield MFTA. Meanwhile, the supernatant was collected to measure the unencapsulated MTO.

The encapsulation efficiency (EE) and drug loading (LC) of MTO were calculated using the following equations:

$$EE\ (\%) = M_t/M_0 \times 100\%$$
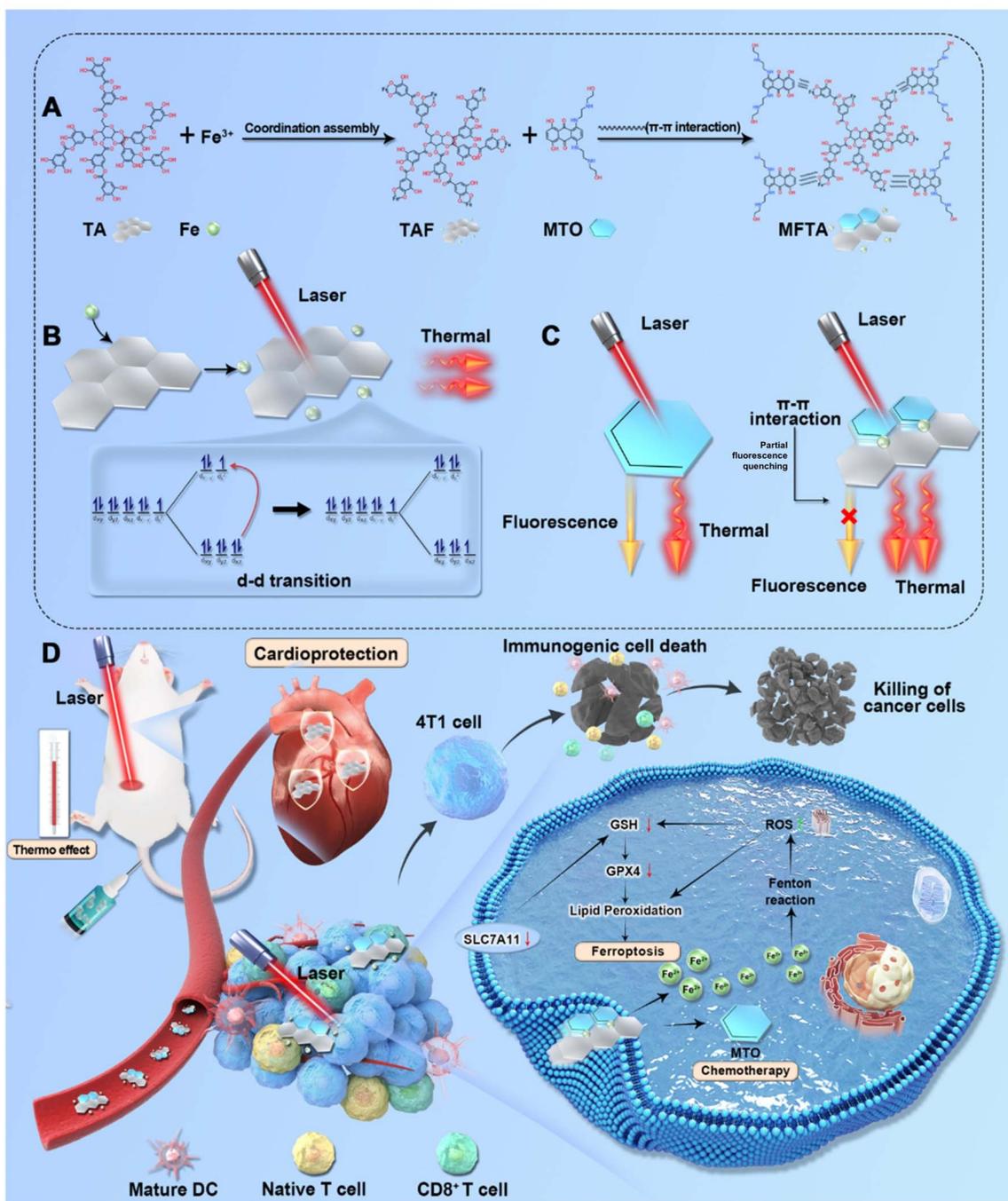
$$LC\ (\%) = M_t/M_L \times 100\%$$

Fig. 1 Schematic illustration of MFTA fabrication and application. (A) Schematic of the synthesis route of MFTA. (B and C) The mechanism of cascade-enhanced photothermal effect in MFTA (D) synergistic therapy by chemo-/photothermal/ferroptosis and immune reaction of TNBC.

where M_t, M_0 and M_L represent the mass of encapsulated MTO, initial MTO and MTO-loaded nanocomposites, respectively. TAF without MTO was synthesized under the same experimental conditions without adding MTO for comparison.

2.3 Characterization of MFTA

Transmission electron microscopy (TEM) imaging was performed using an FEI Tecnai F20 analytical electron microscope (FEI, Hillsborough, Oregon) to examine the size and morphology of MFTA. Element mapping images and energy-dispersive X-ray spectroscopy (EDS) data were also acquired by TEM. A Lambda 25 ultraviolet-visible spectrophotometer was used to capture the spectra.

All samples were distributed in water (0.5 mg mL^{-1}) before testing. The zeta potential and hydrodynamic dimensions were measured with a Malvern Zeta Potentiometer (ZEN3600, UK) and a standard 633 nm laser. All samples were dispersed in water (5 mg mL^{-1}) before determination. To investigate the

stability of MFTA, the nanocomposites were dispersed in water, phosphate-buffered saline (PBS) or cell culture medium (Roswell Park Memorial Institute (RPMI) 1640 medium, 10% fetal bovine serum) at 37 °C for 7 days to determine their hydrodynamic size and zeta potential. Given the weakly acidic tumor environment, MFTA was additionally dispersed in PBS at pH 6.5, 7.4, and 8.5 under the same conditions to determine hydrodynamic size and zeta potential.

The assembly process and characteristics of MFTA were assessed using an X-ray Photoelectron Spectroscopy (XPS, Thermo escalab 250 Xi, USA), a fluorescence spectrometer (RF-5301 PC, Shimadzu, Japan) and Fourier transform infrared spectroscopy (# 6700, Nicolai, USA). Images from a CLSM were captured with an Olympus FV1000 system.

The apoptosis and endocytosis of MFTA by cells were assessed by flow cytometry (FCM; BD LSRFortessa, Becton Dickinson, USA). The effectiveness of PTT was assessed using 808 nm multimode pump laser irradiation (Shanghai Connet Fiber, Shanghai, China). Photoacoustic images were captured with the Vevo LAZR PA system (Visual Sonics, Canada).

2.4 *In vitro* release of MTO

The release of MTO from the MFTA complex was investigated under various situations. First, the MTO release rate of MFTA was investigated at various pH levels (6.5, 7.4 and 8.5). MFTA (0.5 mg) was disseminated in 1 mL of phosphate buffer with a pH of 6.5–8.5. Each dispersion was placed in a dialysis bag (MWCO = 8000 Da) and submerged in an appropriate buffer medium (9 mL). The entire system was kept in a 37 °C thermostatic vibration shaker. About 1 mL of the external phase buffer medium was extracted from various samples at each predetermined time interval and measured at 605 nm using an ultraviolet-visible spectrophotometer, before adding the same volume of a corresponding buffer medium to the external phase. The MTO release triggered by varying power laser irradiation was measured using the same method.

2.5 Analysis of the photothermal properties of MFTA

To investigate the photothermal conversion capability of MFTA *in vitro*, different concentrations of MFTA solution (0.01, 0.05, 0.5 and 1 mg mL^{-1}) were irradiated with an 808 nm laser at 1 W cm^{-2}. Moreover, equivalent concentrations of the MFTA solution were irradiated with different strengths (0, 0.5, 1.0 and 1.5 W cm^{-2}). During the laser irradiation process, the infrared thermal imager was employed to record the changes in temperature of the solution. Finally, the time–temperature curves of MFTA with varied concentrations and MFTA with varying irradiation energies were displayed.

The photothermal stability of MFTA was characterized as follows: MFTA (0.5 mg mL^{-1}) was irradiated with 1.5 W cm^{-2} 808 nm laser and the increase in the temperature of MFTA was continually monitored using an infrared thermal imager. After 10 min of irradiation, the laser was turned off, and the infrared imager continued to monitor the temperature change. Once the temperature of MFTA was reduced to room temperature, it is irradiated again. The process was repeated six times.

2.6 Cell culture and animal experiments

The 4T1 cells obtained from the Chongqing Key Laboratory of Ultrasound Molecular Imaging and Therapy were cultured in RPMI-1640 medium (containing 10% fetal bovine serum and 1% double antibiotics). The cells were cultured under the recommended conditions: 37 °C in a humidified atmosphere with 5% carbon dioxide. All animal procedures were performed in accordance with the Guidelines for Care and Use of Laboratory Animals of Chongqing Medical University and approved by the Institutional Animal Care and Use Committee (IACUC) of Chongqing Medical University.

2.7 Cell uptake experiment

The 4T1 tumor cells were cultured on a 35 mm confocal Petri dish and treated with MFTA nanoplatforms labeled with DiI fluorescent dye for 0.5, 1, 2, 4 and 6 h. The nuclei were stained with DAPI (500 μL, 10 min). The cells were washed three times with PBS and observed using CLSM. For further treatment, the 4T1 tumor cells were cultured in 6-well plates for 24 h and co-incubated with MFTA (0.5 mg mL^{-1}) with tumor cells for 0.5, 1, 2, 4, and 6 h. The cells were then digested and resuspended in PBS. The autofluorescence of intracellular MFTA was detected by FCM.

2.8 *In vitro* and *in vivo* photoacoustic imaging and fluorescence imaging

In vitro photoacoustic imaging of MFTA was performed using a photoacoustic imaging system (Vevo LAZR, Canada) with a photoacoustic gain of 40 dB and an excitation wavelength range of 680–790 nm. Photoacoustic pictures and relative photoacoustic signal values of MFTA at various doses (0.1, 0.25, 0.5, 1, 2.5, 5 mg mL^{-1}) were recorded at the 700 nm wavelength. For *in vivo* PA imaging, tumor-bearing mice ($n = 3$) were intravenously injected with MFTA (5 mg mL^{-1}, 0.1 mL) when the tumor size grew to 160 mm^3. The PA signals arising from the tumor site was recorded at various time-points post-injection.

2.9 Cytotoxicity test

Firstly, the cells were treated with MFTA at gradient concentrations to measure the IC$_{50}$ value of MFTA. Then, a concentration slightly higher than the IC$_{50}$ value was selected as the therapeutic dose for the subsequent experiments. To confirm the synergistic effect of photothermal-chemotherapy of nanoplatforms, the cytotoxicity of different treatment groups at the same MTO concentration was quantified with the CCK8 assay. The 4T1 cells were cultured in 96-well plates at a density of 1×10^4 cells per well. The cells were subsequently separated into six groups: PBS, Laser only, MTO, MFTA, TAF + Laser, and MFTA + Laser. At 24 h post-treatment, cell viability was examined using the conventional CCK-8 assay.

2.10 Cell live-dead staining

The 4T1 tumor cells were seeded in a 35 mm confocal culture dish (2×10^5 per dish) and treated in various treated as follows: PBS, Laser only, MTO, MFTA, TAF + Laser, and MFTA + Laser.

They were washed thrice with PBS, 15 μL of Calcein-AM and 10 μL of PI were added and incubated for 20 min. Finally, they were washed three times with PBS and analyzed using the CLSM system.

2.11 Transcriptome sequencing

RNA sequencing was performed by Qiantang Life Science and Technology Co., Ltd (Suzhou, China). To ensure the reliability and quality of data analysis, the Fastp software was used for quality control of the sequencing data and genome maps. Significant differences were determined according to the thresholds: adjusted p – value < 0.05 and |log 2 (fold change)| > 1. The R software package Deseq2 was used for differential gene expression analysis. The Python package Gseapy was used for Gene Ontology (GO) and Kyoto Encyclopedia of Genes and Genomes (KEGG) pathway enrichment analysis. GO terms or KEGG pathways with p < 0.05 were considered significantly enriched.

2.12 Assessment of apoptosis

The 4T1 cells were seeded in 6-well plates (2×10^5 cells per well) and treated with different treatments as follows: PBS, Laser only, MTO, MFTA, TAF + Laser, and MFTA + Laser. This was followed by digestion with trypsin digestion (Beyotime Biotechnology Co., Ltd), centrifugation at 1000 rpm for 5 min. The precipitate was resuspended in PBS and tagged with Annexin V-FITC and PI (co-incubated for 20 min) for FCM analysis.

2.13 Detection of immunogenic cell death (ICD) *in vitro*

To verify the ICD effect of the nanocomposites on cancer cells, we measured the ATP released. 4T1 cells were cultured on 6-well plates at a density of 2×10^5 cells per well. The cells were then divided into six groups and cultured for 24 h. In this experiment, PBS-treated cells served as controls. The medium from each well was collected used for detection of the ATP concentration using an ATP detection kit following the manufacturer's instructions.

Immunofluorescence labeling was employed to quantify the expression of CRT on the surface of cancer cells. The 4T1 cells were cultured on confocal culture dishes at a density of 2×10^5 cells per dish. The cells were divided into 6 groups, in which PBS-treated cells served as controls.

Following a 24-hour culture, the cells were washed three times with PBS and fixed with 2.5% glutaraldehyde for 15 min. This was followed by rinsing with PBS followed by incubation with FITC-labeled secondary antibody for 60 min. Finally, the cells were stained with DAPI for 15 min at 37 °C and examined under the CLSM.

2.14 Detection of ferroptosis *in vitro*

A hydrogen peroxide detection kit was used to determine the production of hydroxyl radicals ($\cdot$OH) in each treatment group by colorimetric method. The Fe^{2+} group served as the positive

control, and the absorbance values were read using a microplate reader to complete the detection.

DCFH-DA staining was conducted to quantify the levels of ROS. 4T1 cells were cultured on confocal culture dishes at a density of 2×10^5 cells per dish. The participants were divided into 6 groups: PBS, Laser only, MTO, MFTA, TAF + Laser and MFTA + Laser. After 12 h incubation, they were stained with fluorescent DCFH-DA for 20 min. They were then imaged using the CLSM system and analyzed using FCM.

The GSH/GSSG detection kit was used to quantify the levels of GSH in 4T1 cells after exposure to various treatments. The 4T1 cells were cultured in 6-well plates at a density of 2×10^5 cells per well and incubated for 24 h. The cells were divided into 6 distinct groups and incubated for 12 h. They were digested, collected and subjected to the various assays to measure the intracellular GSH level following the instructions on the kit. The intracellular GSH level in 4T1 cells treated with PBS was set to 100%. In addition, the content of GPX4 was detected using ELISA.

The level of lipid peroxide (LPO) in 4T1 cells treated with different treatments was measured using the C11-BODIPY fluorescent probe. The 4T1 cells were cultured in a confocal culture dish at a density of 2×10^5 cells per dish, and cultured with 1 mL of culture media overnight. The cells were then treated in six distinct groups and incubated for 6 h. Following that, the cells were washed three times with PBS and stained with C11-BODIPY for 20 min. The cells were then rinsed three times with PBS, fixed with glutaraldehyde (2.5% for 15 min), stained with DAPI at 37 °C for 15 min, and examined using CLSM. In addition, FCM and ELISA assays were conducted to detect the level of LPO.

2.15 Anti-tumor therapy *in vivo*

The 4T1 tumor-bearing mice were randomly assigned to 6 treatment groups ($n = 5$) as follows: PBS, Laser only, MTO, MFTA, TAF + Laser, and MFTA + Laser. When the tumor volume reached 100 mm^3, anti-tumor treatments were administered. On days 0 and 3, mice were injected with PBS, MTO, TAF or MFTA (100 μL PBS, 5 mg mL^{-1}) *via* the tail vein. The laser irradiation groups received photothermal therapy (1 W cm^{-2}, 10 min) 24 h post-injection.

The tumor volume and body weight of each mouse were measured every 2 days for 14 days. The tumor volume (V) was calculated using the formula: $V = L \times W^2/2$, with L and W representing the tumor's longest and shortest diameters, respectively. The relative tumor volume and relative body weight were calculated using the mice's tumor volume and body weight on the first day.

2.16 Detection of anti-tumor immune response *in vivo*

After 14 days of treatment, the tumor-bearing mice were euthanized, and their spleens and inguinal lymph nodes were collected. Subsequently, the spleens and lymph node tissues were homogenized to prepare single-cell suspensions. The suspensions were stained with fluorescently labeled antibodies (Anti-CD3-PE, Anti-CD4-APC, and Anti-CD8-FITC) to analyze

splenic lymphocyte subsets *via* FCM, with a focus on determining the proportion of cytotoxic T lymphocytes (CTLs, CD8+ T cells). For dendritic cell (DC) activation analysis, the same cell suspensions were stained with another set of fluorescently labeled antibodies (Anti-CD11c-FITC, Anti-CD80-PE, and Anti-CD86-APC), and FCM was used to assess the proportion of activated DCs in both tumor and lymph node tissues.

2.17 Histology and blood examination *in vivo*

Tumor-bearing mice were euthanized 14 days after injection, and key organs (heart, liver, spleen, lung and kidney) and tumor tissues were excised, fixed overnight in 4% paraformaldehyde, and embedded in paraffin. They were sliced for staining with hematoxylin and eosin (H&E), terminal deoxynucleotidyl transferase-mediated d-UTP nick end labeling (TUNEL) and Ki67. TUNEL and Ki67 staining images were taken to examine the apoptosis and proliferation rates of tumor cells. Tumor tissue slices were stained with HMGB-1 and CD8 for immunofluorescence analysis. In addition, critical organ sections were stained with H&E to examine the histological alterations induced by various treatment options.

To test the biosafety of the proposed treatment regimen, mice in the three groups of healthy Balb/c mice ($n = 3$) were injected with MFTA *via* tail vein. PBS-treated mice served as controls. The animals were sacrificed on days 1, 7 and 14 after the injections. Blood samples were collected into tubes containing heparin anticoagulants for further biochemical analysis. Blood cells were counted using an automatic blood cell counter (BC-2800 Vet analyzer, Mindray, Shenzhen, China). The blood samples were spun at 2000 rpm for 3 min to obtain serum which was subjected to the Servicebio Technology Co., Ltd to analyze the serum biochemical indicators.

To test the myocardial protective effect of MFTA, 6 groups of healthy Balb/c mice ($n = 3$) were assigned into anti-tumor treatment groups and treated for 14 days each. Subsequently, the mice were euthanized, and their hearts were harvested for H&E staining to assess the myocardial pathological changes induced by the different treatments. Blood was collected using the Servicebio Technology Co., Ltd for serum myocardial enzyme spectrum indicators assessment.

2.18 Data statistical analysis

Two-tailed *t* test and one-way Anova analysis of various groups were used for statistical significance test $P < 0.05$ was considered statistically significant. *: $p < 0.05$, **: $p < 0.01$, ***: $p < 0.001$, ****: $p < 0.0001$.

3. Results and discussion

3.1 Preparation and characterization of MFTA nanoplatforms

Based on the principle of molecular self-assembly and the theory of coordination chemistry, the MTO, $FeCl_3$ and TA complex MFTA was successfully synthesized by magnetic stirring and natural evaporation. The MFTA aqueous solution (0.5 mg mL^{-1}) was blue-black at room temperature.

Transmission electron microscopy (TEM) images showed that MFTA nanoplatforms exhibited an irregular network structure (Fig. 2A and B), which is consistent with the morphology of metal-phenolic networks characterized in previous studies.[30] To ensure the reliability of the morphological image presented in Fig. 2A, further TEM observations were conducted on the sample with a low concentration of MFTA (0.05 mg mL^{-1}, Fig. S14). The results obtained are essentially consistent. This distinct morphological trait was induced by chaotic stacking during self-assembly. Such irregular anisotropic nanoplatforms are more likely to generate enhanced permeability and retention (EPR) effects because they can roll through blood arteries and penetrate tumor tissue from tumor vasculature with loose endothelial cells.[31] The average particle size and zeta potential of MFTA was 167.00 ± 1.22 nm and -33.13 ± 0.97 mV, respectively. The average particle size and zeta potential of MTO@TA was 123.90 ± 3.02 nm and -18.80 ± 0.82 mV, respectively. And the particle sizes and zeta potential of TAF was 273.40 ± 7.35 nm and -20.90 ± 0.92 mV, respectively (Fig. 2C, D and S13). It can be seen that the particle size of TAF is larger. This is because the formation of hydrogen bonds between the original carboxyl group and the phenolic hydroxyl group of TA contributed to the stability in the aqueous solution. Fe^{3+} occupies the position of the phenolic hydroxyl group in the complex TAF formed after the introduction of Fe ions and destroys some hydrogen bonds, resulting in aggregation between TAF monomers and an increase in particle size.[32] π–π interaction between MTO and TAF prevented the aggregation of TAF after the introduction of MTO, thereby reducing the particle size of MFTA and enhancing the stability of the nanoplatform.[33,34] It is worth noting that due to the irregular shape of the MFTA monomers shown in the TEM images, there is a certain discrepancy between the particle size results measured by DLS and the intuitive results of the TEM images.[35] In summary, during the preparation of MFTA, MTO first forms a stable core complex with $FeCl_3$ through coordinate bonds. Subsequently, this complex assembles into a networked TA structure *via* π–π stacking interactions with TA, following a logic similar to the preparation of core–shell structures, thereby encapsulating MTO inside. Similar MPN structures have also been reported in the literature.[36,37] Meanwhile, the self-assembly based on coordinate bonds and π–π stacking interactions enables MTO to be embedded into the irregular nano-network structure of MFTA.

In addition, under the same experimental conditions, the input ratio of MTO and Fe had a certain effect on the encapsulation efficiency and drug loading rate of the nanoplatforms (Fig. S1, S2 and S17). This may be because too much MTO or too much Fe tends to form more MTO@TA or TAF, which is not conducive to the synthesis of MFTA. To ensure the best encapsulation efficiency and drug loading rate, MTO : $FeCl_3$ at a molar ratio of 1 : 1 was finally chosen for the subsequent synthesis of nanoplatforms. The average particle size and zeta potential of MFTA did not change significantly within 7 days across various simulated physiological environments, indicating that the nanoplatforms possessed good stability and dispersibility (Fig. S3, S4, S15 and S16).
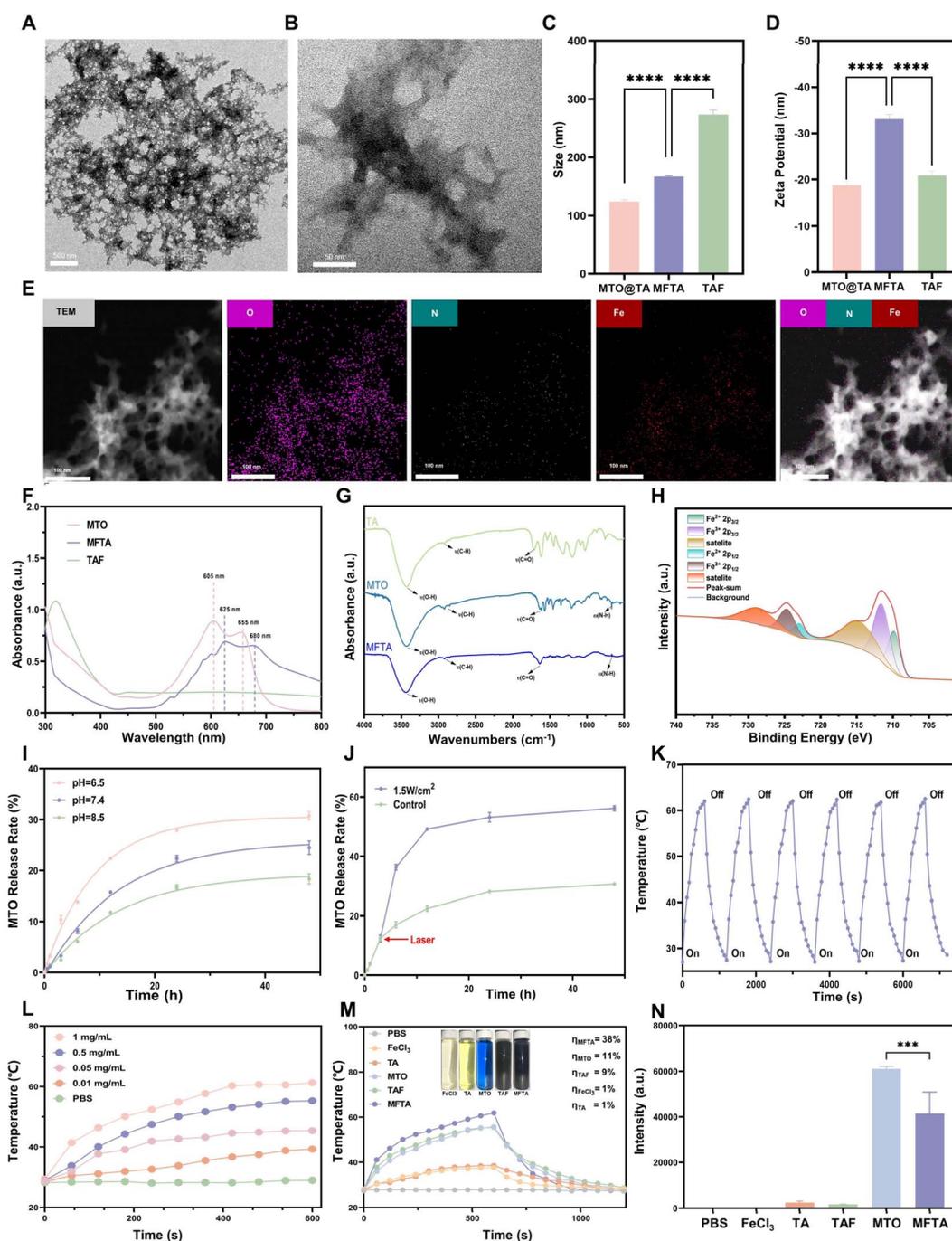
Fig. 2 Characterization of MFTA. (A) TEM image of MFTA. (B) TEM image of MFTA. (C) Size distribution of MTO@TA,MFTA,and TAF ($n = 3$). (D) Zeta potential of MTO@TA,MFTA,and TAF ($n = 3$). (E) Element mapping of MFTA. (F) UV-vis absorbance spectra of MFTA, MTO and TAF. (G) The FTIR spectrum of different samples including MFTA, MTO and TAF. (H) The XPS analysis of MFTA. (I) Cumulative MTO release from MFTA at pH 6.5, 7.4 or 8.5. (J) Cumulative MTO release from MFTA with or without laser irradiation. (K) Temperature elevation curves of MFTA with laser on/off. (L) Temperature elevation curves of MFTA at various concentrations. (M) Photothermal conversion efficiency of MFTA, MTO, TAF, TA and FeCl₃. (N) Fluorescence intensity of MFTA, MTO, TAF, TA and FeCl₃.

The distribution of nitrogen (N), oxygen and Fe in nanoplatforms was characterized by elemental energy spectrum surface scanning (Fig. 2E). Notably, since the composition of TA does not contain N, N can be used as the signal for the successful loading of MTO. Ultraviolet-visible (UV-Vis)

absorption spectra showed that TAF had no special absorption peak in the visible light band, MTO had absorption peaks at about 605 and 655 nm and the absorption peaks of MFTA were red-shifted to 625 and 680 nm (Fig. 2F). According to relevant reports, π–π interaction can lead to an increase in electron

delocalization, a decrease in transition energy and eventually a significant red-shift.[38] Therefore, UV-Vis spectroscopy confirmed the successful loading of MTO and the existence of π–π interaction in MFTA. In addition, the Fourier transform infrared spectra of MTO, TAF and MFTA had similar characteristic peaks of each substance, further confirming the successful loading of each substance by MFTA (Fig. 2G). The valence state of Fe in MFTA was determined by X-ray photoelectron spectroscopy, and the results showed that the Fe in MFTA existed in divalent and trivalent forms (Fig. 2H). The production of divalent Fe is mainly due to the partial reduction of Fe^{3+} to Fe^{2+} by reducing TA. Fe^{2+} can react with endogenous high concentrations of hydrogen peroxide (H_2O_2) to initiate ferroptosis.[39]

The release of MTO in MFTA was determined using a dialysis system. The MTO release efficiency of MFTA in different pH environments was further determined based on previously reported pH-responsive drug release characteristics of TA–Fe.[40] MFTA exhibited a rapid drug release rate in a slightly acidic environment (pH = 6.5) (Fig. 2I). Therefore, the effective concentration of MTO can be increased in the acidic environment of the tumor. In addition, MTO was rapidly released before 12 h under neutral conditions after 5 min of 808 nm laser irradiation at 3 h of dialysis initiation, with less release amount at 12–48 h (Fig. 2J), indicating that NIR can trigger MFTA drug release.

3.2 *In vitro* photothermal properties of MFTA nanoparticles

Firstly, the photothermal stability of MFTA (0.5 mg mL^{-1}) was determined using an 808 nm laser with 1.5 W cm^{-2} energy for six action cycles (on-off). The time–temperature curve showed that the peak temperature of MFTA was 62 °C, and the heating performance did not change significantly (Fig. 2K), indicating that MFTA nanoplatforms had good photothermal stability.

Subsequently, the photothermal conversion performance of MFTA was also evaluated. After MFTA (concentration 0.5 mg mL^{-1}) was irradiated by different energy lasers (0.5, 1.0 and 1.5 W cm^{-2}), the time–temperature curve of each group showed that the rising temperature of MFTA was positively correlated with the laser energy (Fig. S5). Besides, MFTA solutions with different concentrations were irradiated by an 808 nm laser (1 W cm^{-2}, 10 min). The time–temperature curve of each group showed that the rising temperature of MFTA was positively correlated with the concentration of MFTA, while the temperature of the saline group did not change significantly (Fig. 2L).

The mechanism by which MFTA improves the photothermal conversion efficiency was further investigated. The photothermal conversion effect of different component solutions with the same concentration (0.5 mg mL^{-1}) were tested. It was found that under the same power density of 808 nm laser irradiation for 10 min, the temperature of PBS solution did not change significantly, the temperature increases of $FeCl_3$ and TA was lower, MTO and TAF had higher photothermal conversion efficiency and the photothermal effect of MFTA was stronger than that of MTO and TAF (Fig. 2M). Meanwhile, the fluorescence intensity of each solution at 685 nm was measured,[41] and

the results showed that the fluorescence intensity of MFTA was significantly lower than that of MTO (Fig. 2N). This may be due to the intramolecular fluorescence quenching caused by π–π interaction of MFTA during laser irradiation.[42,43] It has been reported that fluorescence quenching caused by intermolecular coordination and π–π interaction enhances the non-radiative transition process of molecules, thus improving the photothermal conversion efficiency in nanoplatforms or molecular systems.[44,45] This is consistent with our observations, as the photothermal properties of MFTA were enhanced after fluorescence quenching.

3.3 Evaluation of targeting performance of MFTA

The endocytosis of MFTA in 4T1 cells was detected by a confocal laser scanning microscope (CLSM). MFTA was labeled with DiI (1,1′-dioctadecyl-3,3,3′3′-tetramethylindocarbocyanine perchlorate). After co-incubation for 0.5, 1, 2, 4 and 6 h, the red fluorescence of MFTA-DiI gradually entered the cells, and the red fluorescence intensity increased with an increase in the co-incubation time (0.5–6 h) (Fig. 3A), indicating that 4T1 cells had good endocytosis and time-dependent effect on MFTA. In addition, the autofluorescence intensity of endocytic MTO in 4T1 cells was measured by FCM, which confirmed the results of CLSM (Fig. 3B and C).

Due to the outstanding photothermal conversion performance and structural characteristics of MFTA, photoacoustic images were captured *in vitro* and *in vivo* using a Vevo LAZR photoacoustic imaging system. As an ideal photoacoustic imaging contrast agent, MFTA exhibited an excellent photoacoustic enhancement effect *in vitro*, with an optimum detection wavelength of 690–710 nm. Meanwhile, the *in vitro* photoacoustic imaging (PAI) signal value increased linearly with an increase in concentration (0.1–10 mg mL^{-1}) (Fig. 3F). After intravenous injection, PAI reached the tumor site at 6 h, peaked at 24 h and decreased after 24 h, and PAI signals were detected even at 72 h (Fig. 3D). Quantitative analysis also confirmed this result (Fig. 3E). *In vivo* PAI results showed that MFTA accumulated at the tumor site through its passive targeting behavior and had a suitable residence time of at least 12–24 h, which would be beneficial for PTT, MTO release and real-time observation.

3.4 Evaluation of the therapeutic and ICD effect of MFTA *in vitro*

The conventional cell counting kit-8 (CCK-8) approach was used to assess the *in vitro* therapeutic effect. 4T1 cells were divided into six groups: PBS, Laser only, MTO, MFTA, TAF + Laser and MFTA + Laser (all groups had concentrations of 0.5 mg mL^{-1}). All the laser irradiation groups mentioned had received photothermal therapy (1 W cm^{-2}, 5 min). The therapy effects of Laser only group and the control group were insufficient. TAF + Laser and MFTA + Laser were significantly better than other groups, even MTO, which indicated the dominant effect of PTT in synergistic therapy. Moreover, MFTA + Laser was better than TAF + Laser, exhibited the remarkable synergistic effect of chemotherapy and PTT (Fig. 4A). The IC$_{50}$ of MFTA was
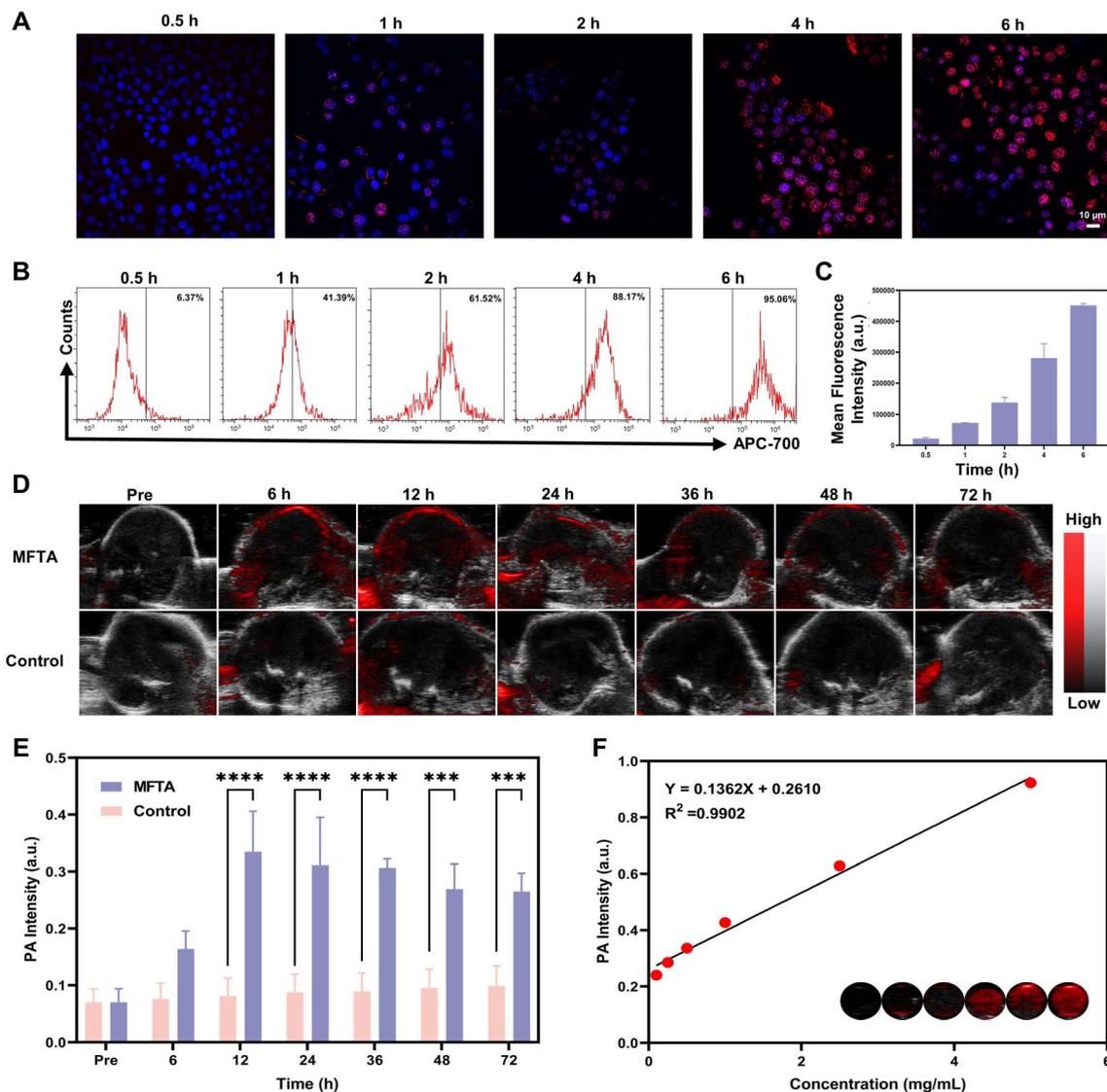
Fig. 3 Targeting performance of MFTA. (A) CLSM images of cell uptake of MFTA. (B) FCM quantification of MFTA uptake by cells. (C) Mean fluorescence intensity in each group ($n = 3$). (D) PA images of tumors. (E) The corresponding signal intensities ($n = 3$). (F) Linear relationship between PA intensities and MFTA concentrations and the corresponding *in vitro* PA images (inset). ***$p < 0.001$, ****$p < 0.0001$.

determined to be 0.48 mg mL^{-1} by the CCK-8 method (Fig. 4B). For subsequent experiments, a concentration slightly higher than the IC$_{50}$ (0.5 mg mL^{-1}) was selected as the therapeutic dosage of MFTA. Different laser intensities (0, 0.5, 1.0 and 1.5 W cm^{-2}) and MFTA concentrations (0, 0.25, 0.5, 1, 2.5, 5 and 10 mg mL^{-1}) were used to further examine the effect of combination therapy. The cell survival rate dropped with an increase in MFTA concentration and laser intensity. The cell survival rate was less than 20% when the MFTA concentration and laser intensity reached 1 mg mL^{-1} and 1.5 W cm^{-2}, respectively (Fig. S6).

4T1 cells in the six groups were treated as previously described to further explore the potential therapeutic effect of nanoplatforms *in vitro*. Propidium iodide (PI, red fluorescence) was used to label dead cells, while Calcein-AM (green fluorescence) was used to stain live cells. According to CLSM observation, the MFTA + Laser group exhibited the greatest

therapeutic effect, in line with the results of the CCK-8 experiment, reinforcing the notion that 4T1 cells respond best to synergistic treatment (Fig. 4D). Apoptosis was assessed *in vitro* using FCM. The treated 4T1 cells were stained with PI and Annexin V-fluorescein isothiocyanate (FITC) before FCM analysis. Apoptosis rate of MTO was higher than Control and Laser only, induced by its chemotherapy effect. Compared with MTO, TAF + Laser had a higher apoptosis rate (Fig. 4E), which further verifies the dominant role of PTT in synergetic therapy. And MFTA + Laser was even significantly higher than TAF + Laser, which further demonstrated an ideal synergistic effect from MFTA. Based on above results, synergistic therapy of MFTA + Laser can effectively induce TNBC cells apoptosis, which is the premise of inducing ICD, and the ICD effect was detected in subsequent experiments.
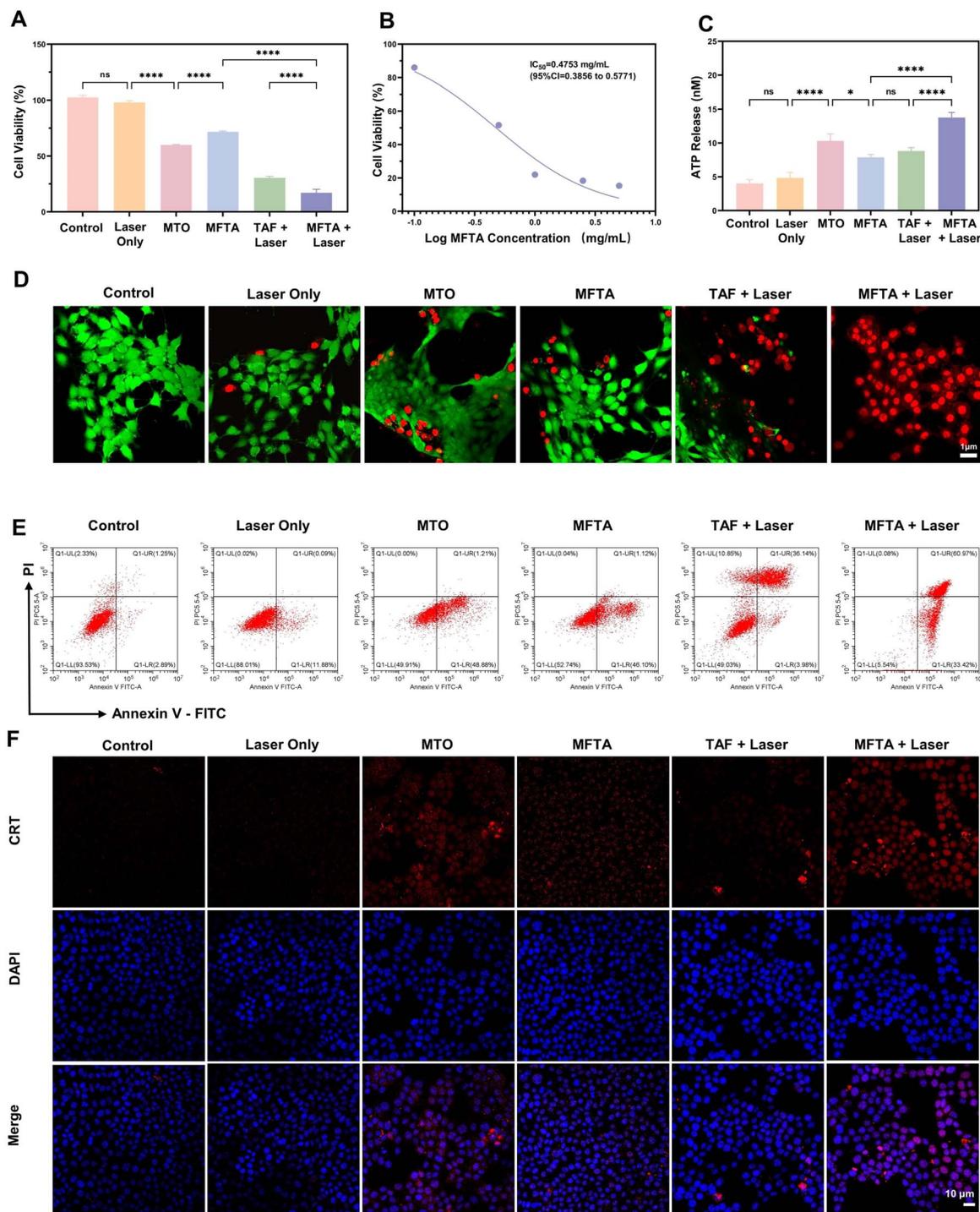
Fig. 4 *In vitro* therapeutic and ICD effects of MFTA. (A) CCK8 results after various treatments ($n = 3$). (B) The IC_{50} value was obtained by plotting a logarithmic fitting curve based on the CCK-8 data. (C) The ATP levels of different treatment groups. (D) CLSM images of 4T1 cells co-stained with CAM and PI after various treatments to distinguish the live (green fluorescence) and dead (red fluorescence) cells. (E) FCM results after various treatments. (F) Immunofluorescence detection of CRT expressed on the surface of 4T1 cells as observed by CLSM. *$p < 0.05$, **$p < 0.01$, ***$p < 0.001$, ****$p < 0.0001$.

Further whole-transcriptome analysis was conducted to comprehensively elucidate the effects of MFTA + Laser on 4T1 cells. Notably, sample correlation analysis was first performed to ensure the reliability of the sequencing results, which showed

high stability and data quality throughout the detection process (Fig. S7A). The correlation coefficients between samples within each group were ≥ 0.99, indicating good reproducibility. This process ensured the reliable identification of differentially
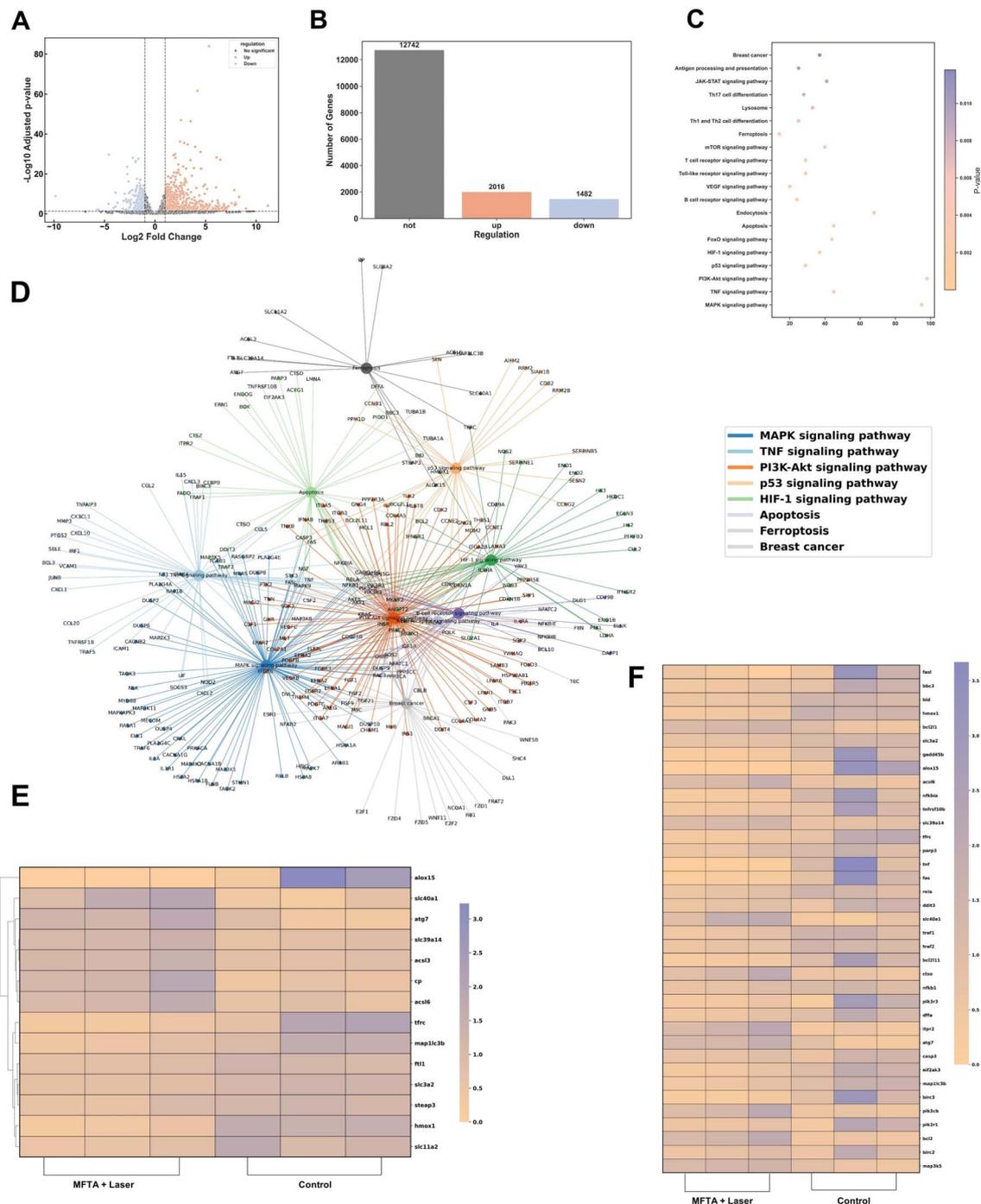
Fig. 5 Transcriptome analysis. (A) Volcano plot of differentially expressed genes between the control and MFTA + laser groups. (B) Statistics of differentially expressed genes between the control group and the MFTA + laser group. (C) KEGG enrichment analysis. (D) Differential gene relationship network associated with each enriched pathway. (E) Cluster heat map showing the differentially expressed genes related to the ferroptosis pathway. (F) Heat map showing the differentially expressed genes related to ferroptosis and apoptosis.

expressed genes. Significantly differentially expressed genes (DEGs) were selected according to the threshold conditions and visualized using a volcano plot (Fig. 5A). Compared with the control group, the expression levels of 3498 genes (2016 up – regulated and 1482 down – regulated) in the MFTA + Laser group changed significantly (Fig. 5B). GO functional classification (Fig. S7B) further revealed that these DEGs were involved in

various biological processes, such as "Intrinsic Apoptotic Signaling Pathway", "Regulation of Alpha–Beta T Cell Differentiation", "Positive Regulation of Natural Killer Cell Mediated Immune Response to Tumor Cell", and "Regulation of Innate Immune Response". KEGG analysis showed that MFTA + Laser significantly activated apoptosis- and ferroptosis-related pathways and triggered immune signaling pathways, including the

"T cell receptor signaling pathway" and the "B cell receptor signaling pathway" (Fig. 5C and D). The heatmaps showed the expression of ferroptosis and apoptosis-related genes in the samples (Fig. 5E and F). These results indicate that MFTA + Laser can induce apoptosis and ferroptosis processes in 4T1 cells and promote tumor-related immune responses to a certain extent.

In summary, the MFTA + Laser group exhibited the most significant therapeutic effect because it enhances photothermal conversion through $\pi-\pi$ interactions, and laser irradiation promotes the release of MTO to achieve chemo-photothermal synergy. TA reduces Fe^{3+} to generate Fe^{2+}, triggering ferroptosis, while inducing ICD to activate immune responses. In addition, the targeted accumulation and precise release of MFTA further improve the therapeutic efficacy. The synergistic effect of multiple mechanisms leads to the optimal therapeutic outcome.

3.5 ICD effect of MFTA *in vitro*

Based on previous experimental data, we hypothesized that synergistic therapy might induce immunogenic cell death (ICD). Therefore, we investigated the specific markers of ICD in 4T1 cells after co-incubation with MFTA, including the release of adenosine triphosphate (ATP), lactate dehydrogenase (LDH), and HMGB-1, as well as the expression of calreticulin (CRT) on the cell surface, to clarify the ICD effect generated by MFTA-mediated apoptosis of triple-negative breast cancer (TNBC) cells.

As previously described, we first evaluated the extracellular ATP, LDH and HMGB1 levels. Compared with the TAF + Laser group and MTO group, the MFTA + Laser group significantly promoted the release of ATP and HMGB1 (Fig. 4C and S20). In addition, LDH, as a marker of cell membrane damage, showed a trend basically consistent with that of cell apoptosis (Fig. S21). We further verified the expression of CRT on the surface of 4T1 cells after various treatments through immunofluorescence staining. Compared with the PBS group, the MTO group, MFTA group, and TAF + Laser group all increased the expression level of CRT on the cell surface to a certain extent. Moreover, the red fluorescent signal of CRT was the strongest in the MFTA + Laser group (Fig. 4F).

Results indicated the MFTA + Laser group had the strongest ICD-inducing activity, co-mediated by MTO, ferroptosis, and photothermal effect. Consistent with group comparisons and literature,[46] we speculate MTO contributes most to ICD induction. MTO's chemotherapeutic effect, together with Fe^{2+}-triggered ferroptosis and TAF's laser-induced photothermal effect, collectively promoted the release of DAMPs and exposure of CRT, ultimately activating ICD. Overall, these results indicated that MFTA synergistic therapy can effectively induce ICD in TNBC cells and initiate anti-tumor immune responses.

3.6 Evaluation of ferroptosis induction effect of MFTA *in vitro*

The ·OH production testing results showed that the ·OH production in iron-containing groups (MFTA, TAF + Laser,

MFTA + Laser) was significantly higher than that in other groups (Fig. S19), indicating that MFTA can effectively induce the Fenton reaction. These results further support its ferroptosis-inducing mechanism.

Subsequently, the mechanism by which MFTA synergistic treatment induces ferroptosis *in vitro* was further investigated. The intracellular glutathione (GSH) level was assessed using the GSH/oxidized glutathione disulfide (GSSG) detection kit following the incubation of various nanomaterials with 4T1 cells. Intracellular GSH can be oxidized by ROS to produce GSSG, which causes the depletion of GSH. The intracellular GSH level of 4T1 cells exposed to laser only was similar to that of the PBS control group. It was observed that the ability to deplete GSH was greatest in the MFTA + Laser group, owing to its most potent photothermal effect (Fig. 6A). Likewise, ELISA results supported the significant up regulation of LPO and down regulation of GPX4 after MFTA + Laser treatment (Fig. 6B and C).

ROS is also closely related to the ferroptosis process, and FCM and CLSM were used to assess the ROS levels in 4T1 cells following various treatments. The generation of intracellular ROS was verified using the ROS-sensitive fluorescent probe 4′,6-diamidino-2-phenylindole (DAPI) and 2,7-dichlorofluorescein diacetate (DCFH-DA). Results showed that 4T1 cells treated with laser only did not significantly alter their ROS levels compared with the PBS control group. It was observed that the TAF + Laser treatment led to an elevation in ROS levels within 4T1 cells. Notably, the MFTA + Laser group generated the highest amount of ROS among all groups, and this finding was in line with the trend of GSH depletion (Fig. 6D and E). Taken together, these findings imply that PTT is the primary contributor to the generation of ROS.

ROS generation leads to the oxidation of GSH to GSSG, reducing the cellular GSH pool. The decrease in GSH levels, in turn, affects the activity of GPX4, which is unable to prevent the accumulation of LPO, ultimately leading to ferroptosis. Since GPX4 can prevent lipid peroxidation (LPO) from converting into fatty alcohols, we examined LPO levels in 4T1 cells following various treatments using CLSM imaging and FCM. A fluorescent probe, C11BODIPY, was employed to detect green fluorescence in LPO-accumulating cells. It was observed that 4T1 cells subjected to MFTA + Laser treatment emitted the most intense green fluorescence signal among all experimental groups (Fig. 6F and S8). This outcome strongly implies that the MFTA + Laser combination down – regulates the expression of GPX4, thereby resulting in the accumulation of LPO. Notably, this finding is in complete accordance with the results derived from the ELISA assay. Furthermore, data obtained from CLSM and FCM clearly demonstrated that the mitochondrial membrane potential, as stained by JC-1, underwent a dramatic decrease subsequent to MFTA + Laser treatment (Fig. 6F and S9). This phenomenon can be attributed to the structural impairment caused by MFTA + Laser, ultimately leading to mitochondrial depolarization. Significantly, the mitochondrial damage induced by ROS renders the cells far more susceptible to ferroptosis.
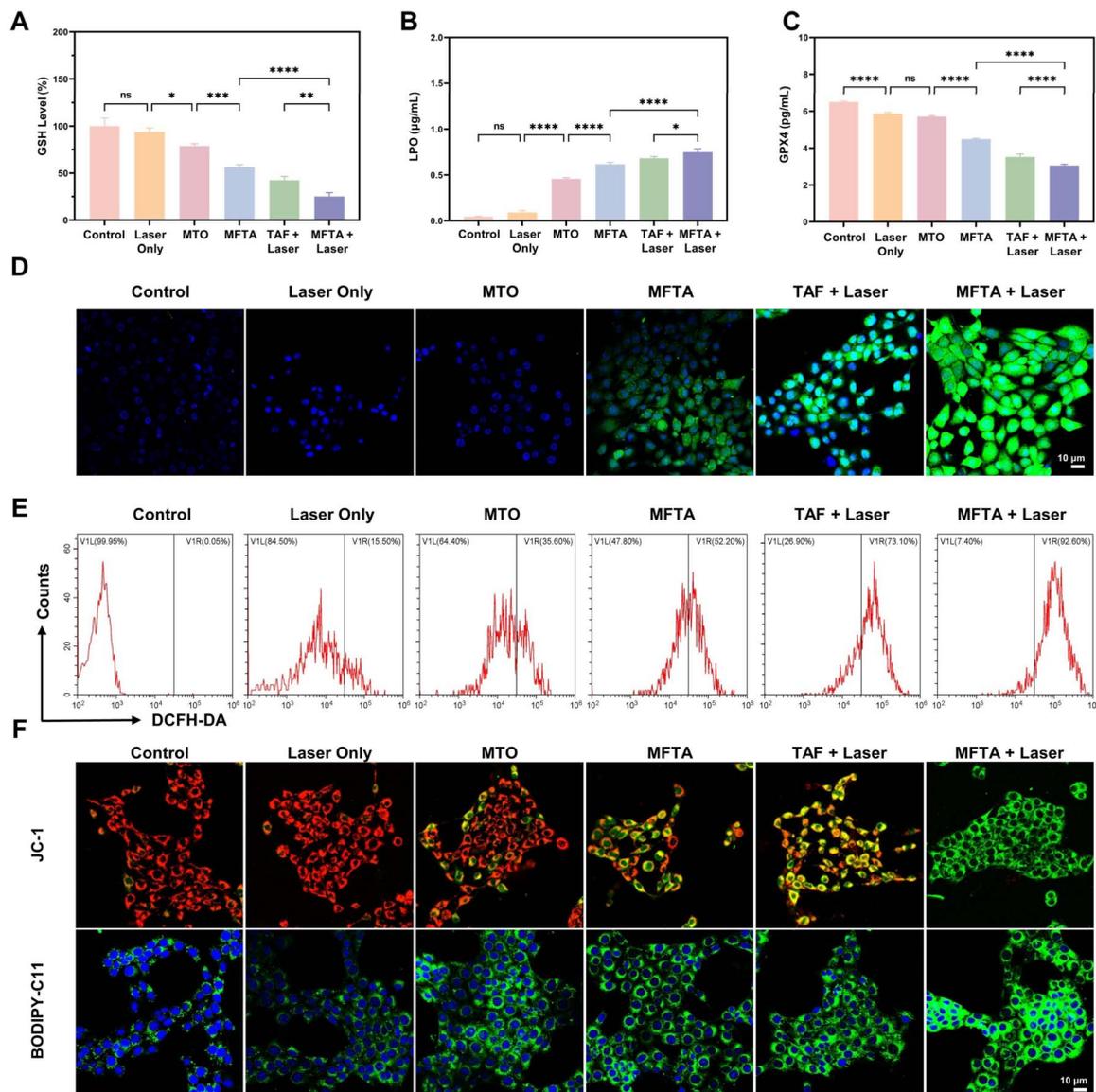
Fig. 6 Ferroptosis induction effect of MFTA *in vitro*. The GSH (A), LPO (B), and GPX4 (C) contents in 4T1 cells after various treatments. CLSM (D) and FCM (E) showing the distribution and level of ROS in 4T1 cells after various treatments. (F) JC-1 and BODIPY-C11 staining results observed by CLSM. $*p < 0.05$, $**p < 0.01$, $***p < 0.001$, $****p < 0.0001$.

Collectively, these data imply that MFTA synergistic therapy can induce ROS, which in turn causes mitochondrial damage. This damage, along with the ability to deplete GSH, down-regulate GPX4, and accumulate LPO in tumor cells, ultimately leads to cell death *via* the ferroptosis pathway.

3.7 Evaluation of the therapeutic effect of MFTA *in vivo*

TNBC mice models were used to assess the effects of synergistic photothermal therapy and chemotherapy *in vivo*. A subcutaneous tumor-bearing animal model was established by injecting 4T1 cells into the fourth pair of mammary glands of Balb/c mice. Mice were then randomly assigned to six groups: PBS, Laser only, MTO, MFTA, TAF + Laser and MFTA + Laser. When the tumor expanded to about 1 cm³, mice received different treatments based on their group. Mice in the Laser irradiation groups were exposed to an

808 nm laser (1 W cm⁻², 5 min), and the irradiation was carried out 24 h after intravenous injection (Fig. 7A).

Throughout the 14-days experimental period, the body weights and the tumor volume of the mice in each group were recorded every 2 days. The results demonstrated that, throughout the experiment, the body weights of the mice in all groups, with the exception of the MTO group, remained relatively stable (Fig. 7B). It can be inferred that, as a chemotherapy drug, MTO has a significant impact on the appetite of mice. In contrast, MFTA exhibits minimal side effects. After treatments, mice were sacrificed and tumors were weighed. The MFTA group demonstrated a certain degree of efficacy attributable to the spontaneous cracking of the nanoplatforms and subsequent drug release. Conversely, the Laser-only group exerted negligible effect since it lacked a PTA. The MFTA + Laser group
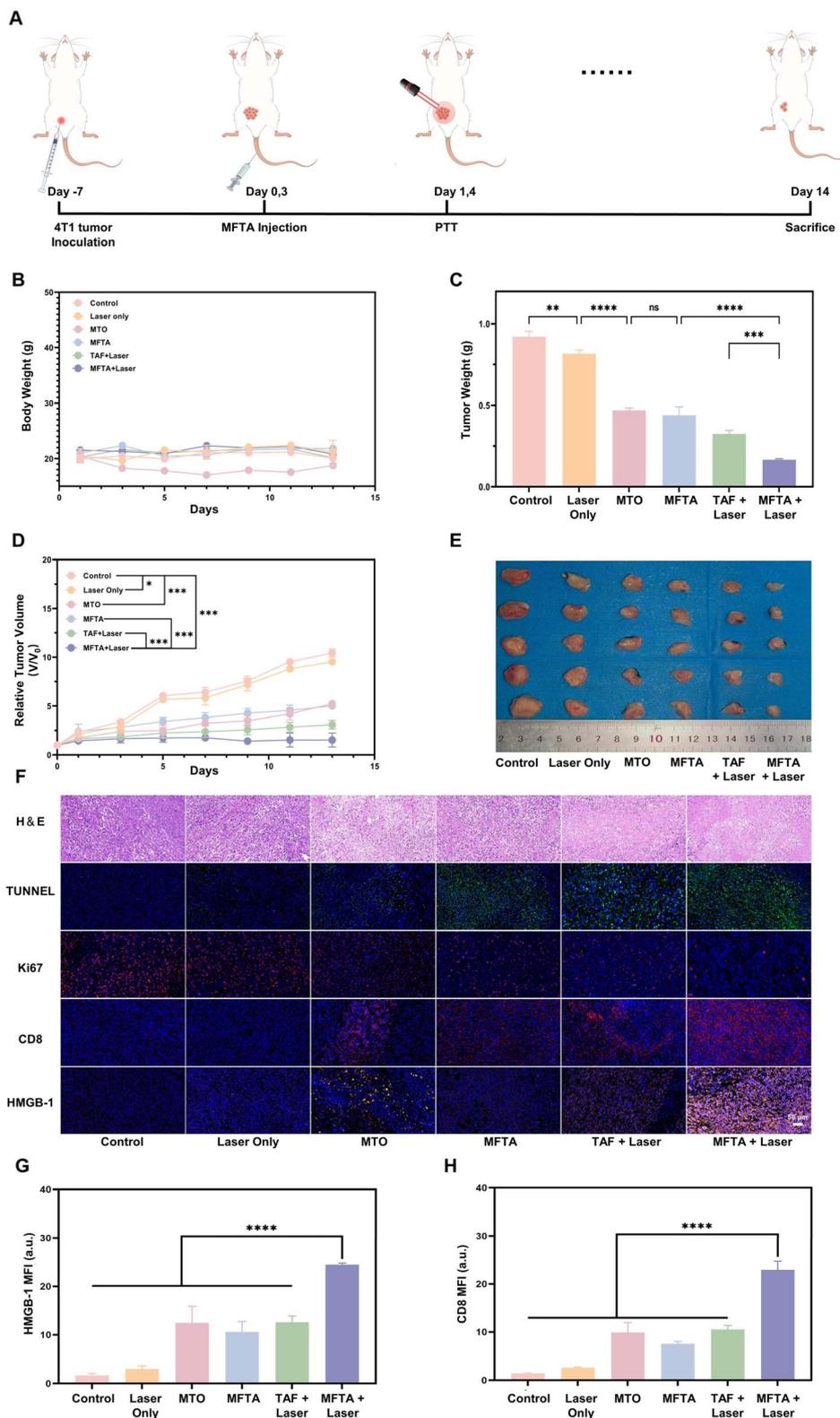
Fig. 7 The therapeutic effect of MFTA *in vivo*. (A) Schematic illustration of the experimental design *in vivo*. (B) Body weight assessments in various treatment groups. (C) Tumor weight. (D) Relative tumor volume. (E) Images of dissected tumors. (F) H&E, Ki67 protein, TUNEL, CD8 and HMGB-1 staining images in tumor tissues after different treatments. CD8 (G) and HMGB-1(H) images from immunofluorescence were quantified with Image J. ****$p < 0.0001$.
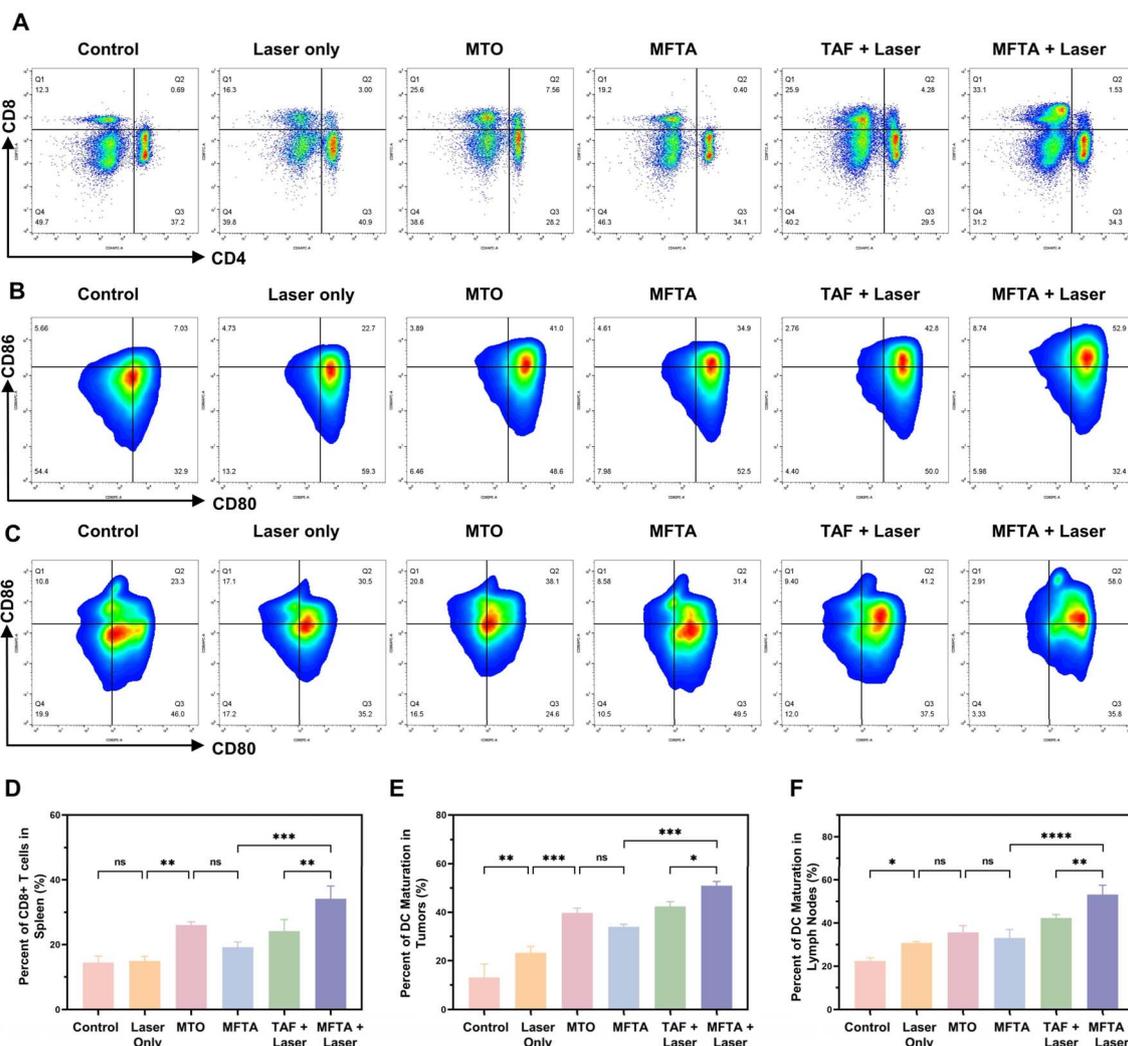
Fig. 8 Evaluation of MFTA-induced specific anti-tumor immunity *in vivo*. (A) FCM analysis of CD8+ T cell populations in spleens. (B) FCM assessment of DC maturation in tumors following various treatments. (C) FCM analysis of DC maturation in regional lymph nodes after different treatments. (D) Quantitative analysis of splenic CD8+ T cell frequencies. (E) Statistical quantification of tumor-infiltrating DC maturation. (F) Quantitative assessment of DC maturation in lymph nodes. *$p < 0.05$, **$p < 0.01$, ***$p < 0.001$, ****$p < 0.0001$.

exhibited the lowest tumor weight, clearly indicating the most favorable therapeutic outcome (Fig. 7C). The trends of tumor volume, both *in vivo* and *in vitro*, were in line with the tumor weight data (Fig. 7D and E).

In addition, hematoxylin and eosin (H&E), terminal deoxynucleotidyl transferase dUTP nick end labeling (TUNEL), and Ki-67 staining were performed to assess the therapeutic efficacy. The staining results confirmed that MFTA + Laser group showed the highest tumor tissue apoptosis/necrosis rate (Fig. 7F) among all groups. Altogether, these results indicate that synergistic therapy has remarkable efficacy in suppressing TNBC tumors.

3.8 Evaluation of MFTA-induced specific anti-tumor immunity

Following the confirmation of ICD at the cellular level, we characterized the dynamics of systemic immune cell responses

in vivo. To evaluate ICD-mediated activation of tumor-infiltrating lymphocytes under the combined therapy of MFTA + Laser, immunofluorescence analysis was performed to quantify the infiltration density of CD8+ T cells and the expression levels of HMGB-1 within tumor tissues.

In the MFTA + Laser group, HMGB-1 expression was significantly upregulated (Fig. 7F and G), demonstrating the potent capacity of this therapeutic regimen to induce ICD. Moreover, this group exhibited the highest degree of CD8+ T cell infiltration into tumors (Fig. 7F and H), underscoring enhanced local immune activation.

Given that tumor cell ICD primes anti-tumor immunity and DC maturation serves as a critical downstream event in ICD-mediated immune activation,[47] FCM was employed to assess DC maturation in both tumor microenvironments and regional inguinal lymph nodes (Fig. 8B and C). While the MTO

monotherapy and TAF + Laser photothermal monotherapy each showed modest DC maturation, the combined therapy of MFTA + Laser induced a statistically significant increase in DC maturation compared to other groups, highlighting its superior ability to promote immune activation (Fig. 8E and F).

Systemic anti-tumor immunity was further evaluated by quantifying splenic CD8+ T lymphocyte counts *via* FCM (Fig. 8A). The MFTA + Laser group showed a marked elevation in splenic CD8+ T cell counts relative to other groups (Fig. 8D), indicating activation of systemic cytotoxic T cell responses – a critical prerequisite for both effective tumor regression and long-term recurrence prevention.[48,49]

3.9 Evaluation of MFTA biocompatibility and myocardial protection effect

The *in vivo* biosafety of MFTA was investigated. MFTA was injected into the healthy mice from tail veins, while the control group received no treatment. Blood samples were collected for biochemical detection (including liver and kidney function) and regular blood analysis before injection as well as on days 1, 7
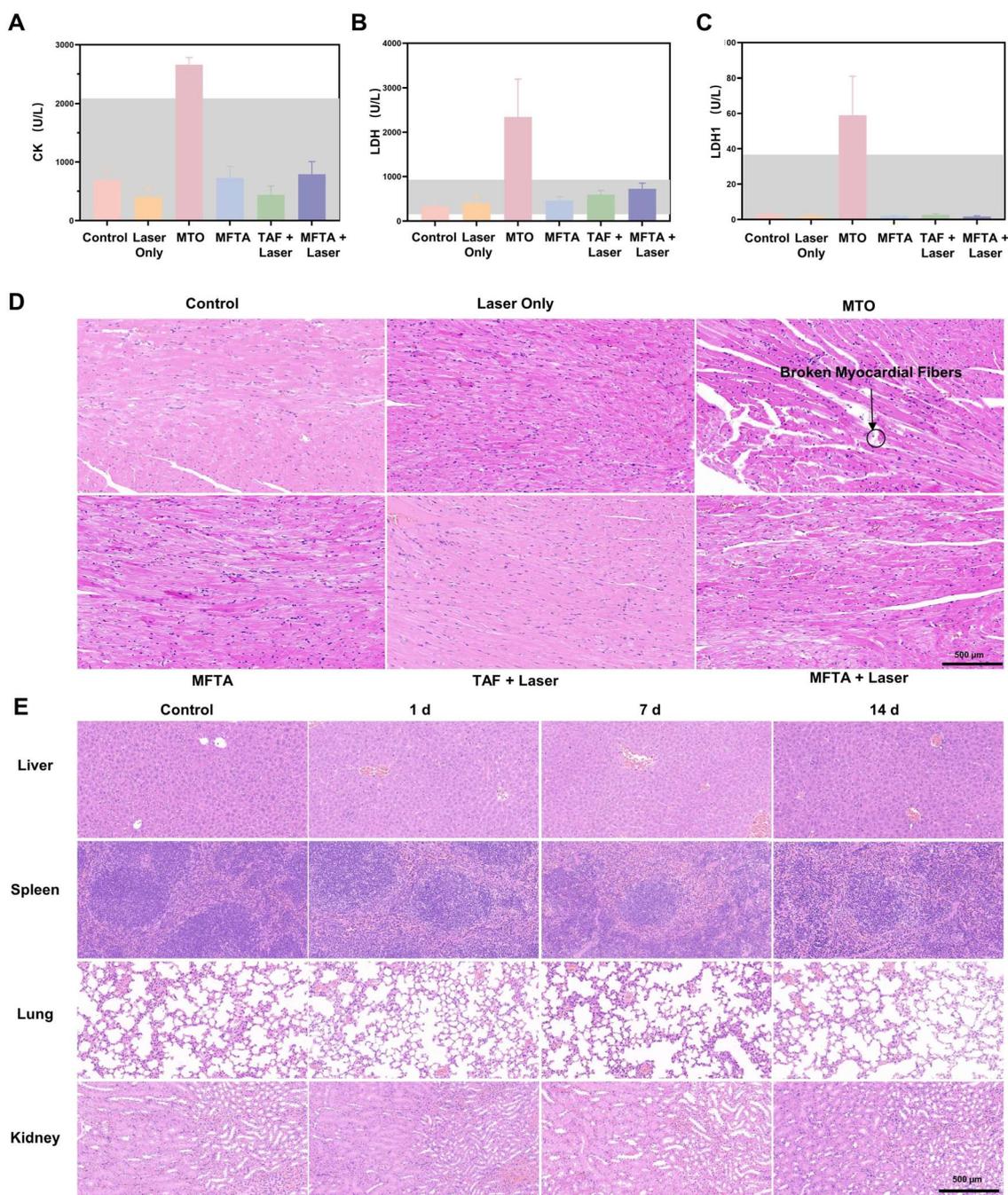
Fig. 9 *In vivo* biosafety assay. (A–C) Results of myocardial enzymes examination. (D) H&E staining of heart tissues after different treatments. (E) H&E staining of the major organ tissues.

and 14 after injection. Meanwhile, the vital organs (including the lung, liver, kidney, and spleen) were dissected for pathological evaluation. No significant differences in blood biochemistry and blood routine indices were found between MFTA and control group after 1, 7 and 14 days of treatment (Fig. S10 and S11). Furthermore, with the normal breast epithelial cell line HC11 as a control, the results showed that the half-maximal inhibitory concentration (IC50) of tumor cells was significantly lower than that of HC11 cells, indicating that MFTA has low toxicity to normal cells (Fig. S18). These results further confirm the safety of MFTA in therapeutic applications.

The removed vital organs were sectioned and stained with H&E. The results showed alveolar epithelial cells, alveolar structures, hepatic lobule structures, glomerular structures, and splenic cords had no significant pathological changes after 1, 7 and 14 days of injection (Fig. 9E). The above hematological and pathological examination results all suggested the good biosafety of MFTA. Notably, previous reports demonstrated that a large dose (75 mg per kg per mouse) of free Fe required for effective ferroptosis may lead to fatal toxicity, especially typical renal injury.[50–52] The serum free iron was also detected after 1, 7 and 14 days of injection in this study, and the results were at a low level (Fig. S12). Additionally, the renal histological and functional detection were normal, indicating the good renal safety.

Finally, the cardioprotective effect of MFTA was separately evaluated in detail. Through H&E staining, myocardial injury was observed in MTO group, manifested as disordered arrangement and rupture of myocardial fibers. Conversely, no significant cardiac pathological changes were found in the MFTA and MFTA + Laser groups (Fig. 9D). This was further confirmed by the results of myocardial enzymes (Fig. 9A–C). These findings imply that MFTA antagonized the cardiotoxicity of MTO through TA, thereby improving the safety of MTO *in vivo*.

Collectively, these results indicate that MFTA has good *in vitro* biocompatibility and *in vivo* biosafety and has the necessary prerequisite for clinical transformation.

4. Conclusion

In conclusion, the multifunctional nanoplatform MFTA developed in this study demonstrates favorable photothermal conversion efficiency and photoacoustic imaging capabilities, enabling good diagnosis and treatment. By integrating PTT, chemotherapy, and ferroptosis strategies, MFTA effectively suppressed tumor growth through synergistic mechanisms. Additionally, MFTA boosted the anti-tumor immune response by inducing ICD, thereby activating the immune system. Importantly, the incorporation of TA in MFTA alleviated MTO-related cardiotoxicity by inhibiting oxidative stress and apoptosis, enhancing its safety profile. Naturally, the design and research of this nanoplatform do have certain limitations: First, it lacks an active targeting mechanism designed for TNBC; second, this study only involves preliminary exploration in terms of ICD; and third, further in-depth investigation is still required in subsequent studies regarding aspects such as long-

term anti-tumor metastasis. Overall, MFTA provides a new strategy for improving the therapeutic effect of TNBC and demonstrates certain application potential.

Author contributions

The manuscript was written through contributions of all authors. All authors have given approval to the final version of the manuscript. Bohao Peng: writing – review & editing, writing – original draft, data curation. Ruoyao Wang: writing – original draft, formal analysis, data curation. Tian Li: methodology. Xiaoqing Yu: software, resources, methodology. Zhiyu Wang: visualization, resources. Xiyang Zhang: methodology. Yuanfeng Tan: methodology. Long Cheng: writing – review & editing, conceptualization. Lu Yang: writing – review & editing, funding acquisition, conceptualization.

Conflicts of interest

There are no conflicts to declare.

Data availability

Data for this article are available at Zenodo at https://doi.org/10.5281/zenodo.15593049.

Supplementary data on material characterization, safety, and related mechanism studies. See DOI: https://doi.org/10.1039/d5ra03962b.

Acknowledgements

References

1 R. L. Siegel, A. N. Giaquinto and A. Jemal, Cancer statistics, 2024, *Ca-Cancer J. Clin.*, 2024, **74**(1), 12–49, DOI: **10.3322/caac.21820**.

2 F. Bray, M. Laversanne, H. Sung, *et al.*, Global cancer statistics 2022: GLOBOCAN estimates of incidence and mortality worldwide for 36 cancers in 185 countries, *Ca-Cancer J. Clin.*, 2024, **74**(3), 229–263, DOI: **10.3322/caac.21834**.

3 R. N. Pedersen, B. Ö. Esen, L. Mellemkjær, *et al.*, The Incidence of Breast Cancer Recurrence 10-32 Years After Primary Diagnosis, *J. Natl. Cancer Inst.*, 2022, **114**(3), 391–399, DOI: **10.1093/jnci/djab202**.

4 R. Dent, M. Trudeau, K. I. Pritchard, *et al.*, Triple-Negative Breast Cancer: Clinical Features and Patterns of Recurrence, *Clin. Cancer Res.*, 2007, **13**(15), 4429–4434, DOI: **10.1158/1078-0432.CCR-06-3045**.

5 G. Bianchini, C. De Angelis, L. Licata and L. Gianni, Treatment landscape of triple-negative breast cancer -

expanded options, evolving needs, *Nat. Rev. Clin. Oncol.*, 2022, **19**(2), 91–113, DOI: **10.1038/s41571-021-00565-2**.

6 P. Zagami and L. A. Carey, Triple negative breast cancer: Pitfalls and progress, *npj Breast Cancer*, 2022, **8**(1), 95, DOI: **10.1038/s41523-022-00468-0**.

7 K. T. Sawicki, V. Sala, L. Prever, E. Hirsch, H. Ardehali and A. Ghigo, Preventing and Treating Anthracycline Cardiotoxicity: New Insights, *Annu. Rev. Pharmacol. Toxicol.*, 2021, **61**, 309–332, DOI: **10.1146/annurev-pharmtox-030620-104842**.

8 A. Narezkina, H. K. Narayan and A. E. Zemljic-Harpf, Molecular mechanisms of anthracycline cardiovascular toxicity, *Clin. Sci.*, 2021, **135**(10), 1311–1332, DOI: **10.1042/CS20200301**.

9 W. Wang, D. Zhang, Z. Jiang, X. Zhang, Y. Jiang and Y. Luan, A Nanodrug-Enabled chemosensitization of cancer stem cells against tumor progression and metastasis, *Chem. Eng. J.*, 2023, **477**, 147121, DOI: **10.1016/j.cej.2023.147121**.

10 S. K. Mishra, A. C. Dhadve, A. Mal, *et al.*, Photothermal therapy (PTT) is an effective treatment measure against solid tumors which fails to respond conventional chemo/radiation therapies in clinic, *Biomater. Adv.*, 2022, **143**, 213153, DOI: **10.1016/j.bioadv.2022.213153**.

11 S. Agarwal, D. K. Jangir and R. Mehrotra, Spectroscopic studies of the effects of anticancer drug mitoxantrone interaction with calf-thymus DNA, *J. Photochem. Photobiol., B*, 2013, **120**, 177–182, DOI: **10.1016/j.jphotobiol.2012.11.001**.

12 Y. Wang, J. Zhang, X. Lv, *et al.*, Mitoxantrone as photothermal agents for ultrasound/fluorescence imaging-guided chemo-phototherapy enhanced by intratumoral H2O2-Induced CO, *Biomaterials*, 2020, **252**, 120111, DOI: **10.1016/j.biomaterials.2020.120111**.

13 H. A. Abdulhafez, R. Ali and M. S. Derayea, A simple single jar "on–off fluorescence" designed system for the determination of mitoxantrone using an eosin Y dye in raw powder, vial, and human biofluids, *RSC Adv.*, 2022, **12**(12), 7413–7421, DOI: **10.1039/D2RA00120A**.

14 Y. Wang, G. Xia, M. Tan, M. Wang, Y. Li and H. Wang, H-Dimeric Nanospheres of Amphipathic Squaraine Dye with an 81.2% Photothermal Conversion Efficiency for Photothermal Therapy, *Adv. Funct. Mater.*, 2022, **32**(25), 2113098, DOI: **10.1002/adfm.202113098**.

15 F. Yang, Y. Xiao, J. H. Ding, *et al.*, Ferroptosis heterogeneity in triple-negative breast cancer reveals an innovative immunotherapy combination strategy, *Cell Metab.*, 2023, **35**(1), 84–100, DOI: **10.1016/j.cmet.2022.09.021**.

16 Y. Yu, Z. Huang, Q. Chen, *et al.*, Iron-based nanoscale coordination polymers synergistically induce immunogenic ferroptosis by blocking dihydrofolate reductase for cancer immunotherapy, *Biomaterials*, 2022, **288**, 121724, DOI: **10.1016/j.biomaterials.2022.121724**.

17 T. Liu, W. Liu, M. Zhang, *et al.*, Ferrous-Supply-Regeneration Nanoengineering for Cancer-Cell-Specific Ferroptosis in Combination with Imaging-Guided Photodynamic Therapy, *ACS Nano*, 2018, **12**(12), 12181–12192, DOI: **10.1021/acsnano.8b05860**.

18 J. Qin, G. Liang, Y. Feng, *et al.*, Synthesis of gadolinium/iron–bimetal–phenolic coordination polymer nanoparticles for theranostic applications, *Nanoscale*, 2020, **12**(10), 6096–6103, DOI: **10.1039/C9NR10020B**.

19 J. Zeng, M. Cheng, Y. Wang, *et al.*, pH-Responsive Fe(III)–Gallic Acid Nanoparticles for In Vivo Photoacoustic-Imaging-Guided Photothermal Therapy, *Adv. Healthcare Mater.*, 2016, **5**(7), 772–780, DOI: **10.1002/adhm.201500898**.

20 X. Sui, J. Wang, Z. Zhao, *et al.*, Phenolic compounds induce ferroptosis-like death by promoting hydroxyl radical generation in the Fenton reaction, *Commun. Biol.*, 2024, **7**(1), 199, DOI: **10.1038/s42003-024-05903-5**.

21 Y. Wang, F. Liu, N. Yan, *et al.*, Exploration of FeIII-Phenol Complexes for Photothermal Therapy and Photoacoustic Imaging, *ACS Biomater. Sci. Eng.*, 2019, **5**(9), 4700–4707, DOI: **10.1021/acsbiomaterials.9b00711**.

22 J. Zhang, L. Cui, X. Han, *et al.*, Protective effects of tannic acid on acute doxorubicin-induced cardiotoxicity: Involvement of suppression in oxidative stress, inflammation, and apoptosis, *Biomed. Pharmacother.*, 2017, **93**, 1253–1260, DOI: **10.1016/j.biopha.2017.07.051**.

23 X. Wang, D. Wang, J. Li, M. Zhang and P. Song, Physical Mechanism of Photoinduced Charge Transfer in One- and Two-Photon Absorption in D-D-π-A Systems, *Materials*, 2021, **14**(14), 3925, DOI: **10.3390/ma14143925**.

24 Y. Abderrazak, A. Bhattacharyya and O. Reiser, Visible-Light-Induced Homolysis of Earth-Abundant Metal-Substrate Complexes: A Complementary Activation Strategy in Photoredox Catalysis, *Angew. Chem., Int. Ed.*, 2021, **60**(39), 21100–21115, DOI: **10.1002/anie.202100270**.

25 M. Aioub, S. R. Panikkanvalappil and M. A. El-Sayed, Platinum-Coated Gold Nanorods: Efficient Reactive Oxygen Scavengers That Prevent Oxidative Damage toward Healthy, Untreated Cells during Plasmonic Photothermal Therapy, *ACS Nano*, 2017, **11**(1), 579–586, DOI: **10.1021/acsnano.6b06651**.

26 S. Bai, L. L. Yang, Y. Wang, *et al.*, Prodrug-Based Versatile Nanomedicine for Enhancing Cancer Immunotherapy by Increasing Immunogenic Cell Death, *Small Weinh. Bergstr. Ger.*, 2020, **16**(19), e2000214, DOI: **10.1002/smll.202000214**.

27 Y. Abdou, A. Goudarzi, J. X. Yu, S. Upadhaya, B. Vincent and L. A. Carey, Immunotherapy in triple negative breast cancer: beyond checkpoint inhibitors, *npj Breast Cancer*, 2022, **8**(1), 1–10, DOI: **10.1038/s41523-022-00486-y**.

28 H. Abouali, M. Przedborski, M. Kohandel and M. Poudineh, Investigating nano-sized tumor-derived extracellular vesicles in enhancing anti-PD-1 immunotherapy, *Nanoscale*, 2024, **16**(40), 19062–19073, DOI: **10.1039/d4nr00729h**.

29 C. Chen, X. Ni, S. Jia, *et al.*, Massively Evoking Immunogenic Cell Death by Focused Mitochondrial Oxidative Stress using an AIE Luminogen with a Twisted Molecular Structure, *Adv. Mater.*, 2019, **31**(52), 1904914, DOI: **10.1002/adma.201904914**.

30 H. Xiong, C. Wang, Z. Wang, Z. Jiang, J. Zhou and J. Yao, Intracellular cascade activated nanosystem for improving ER+ breast cancer therapy through attacking GSH-

mediated metabolic vulnerability, *J. Controlled Release*, 2019, **309**, 145–157, DOI: **10.1016/j.jconrel.2019.07.029**.

31 H. Xiong, S. Du, J. Ni, J. Zhou and J. Yao, Mitochondria and nuclei dual-targeted heterogeneous hydroxyapatite nanoparticles for enhancing therapeutic efficacy of doxorubicin, *Biomaterials*, 2016, **94**, 70–83, DOI: **10.1016/j.biomaterials.2016.04.004**.

32 Z. Fu and R. Chen, Study of Complexes of Tannic Acid with Fe(III) and Fe(II), *J. Anal. Methods Chem.*, 2019, **2019**(1), 3894571, DOI: **10.1155/2019/3894571**.

33 S. Toksoz, H. Acar and M. O. Guler, Self-assembled one-dimensional soft nanostructures, *Soft Matter*, 2010, **6**(23), 5839–5849, DOI: **10.1039/C0SM00121J**.

34 Q. Sun, Z. Zhou, N. Qiu and Y. Shen, Rational Design of Cancer Nanomedicine: Nanoproperty Integration and Synchronization, *Adv. Mater.*, 2017, **29**(14), 1606628, DOI: **10.1002/adma.201606628**.

35 R. Mathaes, G. Winter, J. Engert and A. Besheer, Application of different analytical methods for the characterization of non-spherical micro- and nanoparticles, *Int. J. Pharm.*, 2013, **453**(2), 620–629, DOI: **10.1016/j.ijpharm.2013.05.046**.

36 X. Chen, R. Ma, Z. Fu, *et al.*, Metal-phenolic networks-encapsulated cascade amplification delivery nanoparticles overcoming cancer drug resistance via combined starvation/chemodynamic/chemo therapy, *Chem. Eng. J.*, 2022, **442**, 136221, DOI: **10.1016/j.cej.2022.136221**.

37 Z. Lin, J. Zhou, Y. Qu, *et al.*, Luminescent Metal-Phenolic Networks for Multicolor Particle Labeling, *Angew. Chem.*, 2021, **133**(47), 25172–25179, DOI: **10.1002/ange.202108671**.

38 A. M. Smith, R. J. Williams, C. Tang, *et al.*, Fmoc-Diphenylalanine Self Assembles to a Hydrogel via a Novel Architecture Based on π–π Interlocked β-Sheets, *Adv. Mater.*, 2008, **20**(1), 37–41, DOI: **10.1002/adma.200701221**.

39 W. Bao, X. Liu, Y. Lv, *et al.*, Nanolongan with Multiple On-Demand Conversions for Ferroptosis-Apoptosis Combined Anticancer Therapy, *ACS Nano*, 2019, **13**(1), 260–273, DOI: **10.1021/acsnano.8b05602**.

40 M. S. Taha, G. M. Cresswell, J. Park, W. Lee, T. L. Ratliff and Y. Yeo, Sustained Delivery of Carfilzomib by Tannic Acid-Based Nanocapsules Helps Develop Antitumor Immunity, *Nano Lett.*, 2019, **19**(11), 8333–8341, DOI: **10.1021/acs.nanolett.9b04147**.

41 S. Bhunia, P. Saha, P. Moitra, A. M. Addicoat and S. Bhattacharya, Efficacious and sustained release of an anticancer drug mitoxantrone from new covalent organic

frameworks using protein corona, *Chem. Sci.*, 2022, **13**(26), 7920–7932, DOI: **10.1039/D2SC00260D**.

42 W. R. Zhuang, Y. Wang, P. F. Cui, *et al.*, Applications of π-π stacking interactions in the design of drug-delivery systems, *J. Controlled Release*, 2019, **294**, 311–326, DOI: **10.1016/j.jconrel.2018.12.014**.

43 Y. Liang, X. Deng, L. Zhang, *et al.*, Terminal modification of polymeric micelles with π-conjugated moieties for efficient anticancer drug delivery, *Biomaterials*, 2015, **71**, 1–10, DOI: **10.1016/j.biomaterials.2015.08.032**.

44 S. S. Zadeh, A. Ebrahimi and A. Shahraki, The impact of π-π stacking interactions on photo-physical properties of hydroxyanthraquinones, *Spectrochim. Acta, Part A*, 2023, **292**, 122453, DOI: **10.1016/j.saa.2023.122453**.

45 W. Du, Y. Chong, X. Hu, *et al.*, Increasing Photothermal Efficacy by Simultaneous Intra- and Intermolecular Fluorescence Quenching, *Adv. Funct. Mater.*, 2020, **30**(5), 1908073, DOI: **10.1002/adfm.201908073**.

46 A. D. Garg, S. More, N. Rufo, *et al.*, Trial watch: Immunogenic cell death induction by anticancer chemotherapeutics, *Oncoimmunology*, 2017, **6**(12), e1386829, DOI: **10.1080/2162402X.2017.1386829**.

47 A. Del Prete, V. Salvi, A. Soriani, *et al.*, Dendritic cell subsets in cancer immunity and tumor antigen sensing, *Cell. Mol. Immunol.*, 2023, **20**(5), 432–447, DOI: **10.1038/s41423-023-00990-6**.

48 S. Budhu, J. D. Loike, A. Pandolfi, *et al.*, CD8+ T cell concentration determines their efficiency in killing cognate antigen–expressing syngeneic mammalian cells in vitro and in mouse tissues, *J. Exp. Med.*, 2010, **207**(1), 223–235, DOI: **10.1084/jem.20091279**.

49 S. J. Im, M. Hashimoto, M. Y. Gerner, *et al.*, Defining CD8+ T cells that provide the proliferative burst after PD-1 therapy, *Nature*, 2016, **537**(7620), 417–421, DOI: **10.1038/nature19330**.

50 Z. Raza and Z. Naureen, Melatonin ameliorates the drug induced nephrotoxicity: Molecular insights, *Nefrología*, 2020, **40**(1), 12–25, DOI: **10.1016/j.nefro.2019.06.009**.

51 J. Wang, Y. Wang, Y. Liu, *et al.*, Ferroptosis, a new target for treatment of renal injury and fibrosis in a 5/6 nephrectomy-induced CKD rat model, *Cell Death Discov.*, 2022, **8**(1), 1–10, DOI: **10.1038/s41420-022-00931-8**.

52 B. Borawski and J. Malyszko, Iron, ferroptosis, and new insights for prevention in acute kidney injury, *Adv. Med. Sci.*, 2020, **65**(2), 361–370, DOI: **10.1016/j.advms.2020.06.004**.